Prototyping of MISR LAI and FPAR Algorithm with POLDER Data over Africa

Yu Zhang, Yuhong Tian, Yuri Knyazikhin, John V. Martonchik, Dave J. Diner, Marc Leroy, and Ranga B. Myneni

***Abstract*—The multi-angle imaging spectroradiometer (MISR) instrument is designed to provide global imagery at nine discrete viewing angles and four visible/near-infrared spectral bands. The MISR standard products include vegetation canopy green leaf area index (LAI) and fraction of photosynthetically active radiation absorbed by vegetation (FPAR). These products are produced using a peer-reviewed algorithm documented in the EOS-AM1 (Terra) special issue of the *Journal of Geophysical Research*. This paper presents results on spatial distributions of LAI and FPAR of vegetated land surfaces derived from the MISR LAI/FPAR algorithm with bidirectional reflectance data from the polarization and directionality of the Earth's reflectance (POLDER) instrument over Africa. The results indicate that the proposed algorithm reflects the physical relationships between surface reflectances and biophysical parameters and demonstrates the advantages of using multi-angle data instead of single-angle data. A new method for evaluating bihemispherical reflectance (BHR) from multi-angle measurements of hemispherical directional reflectance factor (HDRF) was developed to prototype the algorithm with POLDER data. The accuracy of BHR evaluation and LAI/FPAR estimation is also presented. To demonstrate the advantages of using multi-angle data over single-angle data of surface reflectance, we demonstrate that: 1) the use of multi-angle data can decrease the dispersion and saturation of LAI, and increase the localization and quality of retrieved LAI and FPAR, 2) the use of multi-angle data can improve the accuracy of LAI retrievals in geometrically complex canopies such as shrubs, and 3) the use of multi-angle data can help determine biome or land cover types correctly (by using the minimum value of LAI dispersion). For many other cases, we demonstrate that the use of multi-angle data does not lead to misevaluation, even if the land cover type is misidentified.**

***Index Terms*—Fraction of photosynthetically active radiation absorbed by vegetation (FPAR), leaf area index (LAI), multi-angle imaging spectroradiometer (MISR), multi-angle remote sensing, polarization and directionality of the Earth's reflectance (POLDER), terra.**

I. Introduction

THE multi-angle imaging spectroradiometer (MISR) is an instrument on board the EOS-AM1 platform called Terra. MISR will make global observations of the Earth's surface at 1.1 km spatial resolution with the objective of determining the atmospherically corrected reflectance properties of most of the land surface and the tropical ocean [1]. Two types of atmosphere-corrected bidirectional surface reflectances and their integrated values will be made available from this instrument. The hemispherical directional reflectance factor (HDRF) and the bihemispherical reflectance (BHR) characterize surface reflectance under ambient sky conditions (i.e., direct and diffused illumination). The HDRF and BHR do not depend on surface radiation models used and are highly accurate when correct atmospheric information is used [1]. The bidirectional reflectance factor (BRF) and the directional hemispherical reflectance (DHR) are defined for the unique case when the atmosphere is absent. The removal of the effects of diffuse sky radiance from the HDRF requires the use of a model for the surface bidirectional reflectance distribution function (BRDF). This makes the retrieved BRF and DHR model dependent [2].

An operational algorithm that uses BHR, HDRF, and their uncertainties as input variables was proposed in [2] and [3]. This algorithm is specific to the MISR instrument for the retrieval of green leaf area index (LAI) and fraction of photosynthetically active radiation absorbed by vegetation (FPAR). Prior to the launch of the MISR instrument, the physical credibility and performance of the algorithm needs to be evaluated. Surrogate multi-angle satellite data can be used to accomplish this task, which is termed here as prototyping. The polarization and directionality of the Earth's reflectance (POLDER) sensor was designed to provide global measurements of spectral, directional, and polarizational characteristics of solar radiation reflected by the earth's surface. Atmospherically corrected surface reflectances acquired by POLDER are presently available. The goal for this paper is to prototype the MISR LAI and FPAR algorithm with data acquired by the POLDER instrument over Africa.

A brief description of concepts for the algorithm is given, followed by analysis of vegetation spectral and angular signatures from POLDER data. A series of algorithm prototyping retrievals are presented and discussed in detail. The algorithm clearly demonstrates better results when multi-angle data are used compared to single-angle data, thus indicating both the advantage of multi-angle data and the ability of the algorithm to recognize the enhanced information content in multi-angle data. Finally, a method to evaluate BHR's from POLDER data is proposed and evaluated. It was used to prototype aspects of the MISR algorithm.

II. Algorithm

A. Mathematical Basis for Multi-Angle Remote Sensing of Vegetation

We begin with a theorem recently published in a journal on inverse problems [4]. The theorem states that under general

Manuscript received May 7, 1999; revised March 1, 2000. This work was supported by the National Aeronautics and Space Administration (NASA) MODIS Contract NAS5-96 061 and Jet Propulsion Laboratory MISR Contract 000 960 914.

Y. Zhang, Y. Tian, Y. Knyazikhin, and R. B. Myneni are with the Department of Geography, Boston University, Boston, MA 02215 USA (e-mail: yuzhang@crsa.bu.edu).

J. V. Martonchik and D. J. Diner are with the Jet Propulsion Laboratory, California Institute of Technology, Pasadena, CA 91109 USA.

M. Leroy is with the Centre d'Etudes Spatiales de la Biosphère (CESBIO), Toulouse, France.

Publisher Item Identifier S 0196-2892(00)06225-2.

conditions, the three-dimensional (3-D) extinction coefficient and 3-D scattering phase function can be uniquely retrieved from boundary measurements. This theorem indicates there is a one-to-one correspondence between the complex 3-D vegetation canopy structure and radiation emergent from the canopy boundaries. A question then arises as to whether or not this correspondence can be specified from multi-angle observations. Let us consider a hypothetical ideal instrument that provides exact surface reflectances at any spatial point and in any direction, i.e., one has the complete and accurate spatial and angular information on the radiation field leaving the canopy through the upper boundary. The theorem, however, requires information on the downward radiation field at the canopy bottom boundary to redeem canopy structure. How can we obtain this information?

A specific feature of photon interactions with vegetation elements lies in the fact that the probability a photon will interact with phytoelement is not dependent on wavelength; the extinction coefficient, the sum of wavelength dependent scattering and absorption coefficients, does not depend on wavelength [5]. This allows evaluation of canopy transmittance at any wavelength once this variable is known at a fixed wavelength [6]. Mathematically, the inverse problem of recovering 3-D canopy structure from multi-angle observations can be formulated as the following. Given "ideal" multi-angle canopy reflectances at a minimum of two spectral bands, find the canopy transmittance at a fixed wavelength and canopy structure. This formulation includes two sets of known simultaneous multi-angle data and two sets of unknowns. These data sets relate all variables needed for unique retrieval of the 3-D structure of the medium. Thus, the main advantage of multi-angle remote sensing is its potential ability to retrieve realistic 3-D geophysical parameters required by many interdisciplinary investigations [7]. It is clear that the above arguments need a rigorous mathematical analysis and this is provided elsewhere [3], [4]. These arguments are the basis of the LAI/FPAR retrieval techniques developed for operational use during the EOS Terra mission [3], [6].

The above arguments indicate the canopy radiation model, the foundation of any retrieval technique, must also provide canopy transmittance to obtain a closed system of equations for the solution of the inverse problem. We begin with the representation of monochromatic intensity $I_\lambda(r,\Omega)$ of a 3-D radiative field at wavelength λ at a spatial point r and in direction Ω as a sum of two components, that is

$$I_\lambda(r,\Omega) = I_{\mathrm{bs},\lambda}(r,\Omega) + I_{\mathrm{rest},\lambda}(r,\Omega) \tag{1}$$

where the first component $I_{\mathrm{bs},\lambda}(r,\Omega)$ describes the radiation regime within the vegetation canopy for the case of a black surface at the bottom of the medium, and $I_{\mathrm{rest},\lambda}(r,\Omega)$ describes additional radiative fields due to interactions between the surface and canopy. This representation takes a simple form when the vegetation canopy can be idealized as a horizontally homogeneous medium bounded at the bottom by a Lambertian surface. The term $I_{\mathrm{rest},\lambda}(r,\Omega)$ can be expressed as follows [8]

$$I_{\mathrm{rest},\lambda}(r,\Omega) = \frac{\rho_\lambda}{1-\rho_\lambda R_\lambda} T_{\mathrm{bs},\lambda} I_{S,\lambda} \tag{2}$$

where ρ_λ is the albedo of the Lambertian surface, $T_{\mathrm{bs},\lambda}$ is the downward flux at the surface level (transmittance) for the case of the black surface, $I_{S,\lambda}$ and R_λ are radiance and downward flux at the surface level generated by an isotropic wavelength-independent source located at the canopy bottom. Three independent variables are needed to describe the radiative regime in a plane-parallel medium: the reflectance properties of the surface, which are not dependent upon the vegetation, and $I_{\mathrm{bs},\lambda}$ and $I_{S,\lambda}$, which are surface-independent parameters because no multiple interaction of radiation between the surface and canopy is possible (i.e., these variables have intrinsic canopy information).

More complicated techniques, for example, the adjoint formulation and Green's function concept, have been developed in reactor physics to extend the representations (1) and (2) for the case of a 3-D radiation field [9]. Although in the 3-D case, $I_{\mathrm{rest},\lambda}$ cannot be expressed in such a simple form, the physical meaning of (1) and (2) remains unchanged. That is, the 3-D radiation field can be parameterized in terms of surface reflectance properties that are independent of vegetation such as the radiation field in the vegetation canopy for the case of the black surface ("Black soil problem") and the radiation field in the vegetation canopy generated by anisotropic heterogeneous wavelength-independent sources located at the canopy bottom ("S problem"). This technique was used to create the look-up table (LUT) for the LAI/FPAR algorithm [10]. In terms of this approach, the hemispherical directional reflectance factor (HDRF) $\mathbf{r}_\lambda(\Omega,\Omega_0)$ and bihemispherical reflectance (BHR) $A_\lambda(\Omega_0)$ at wavelength λ can be expressed as

$$\mathbf{r}_\lambda(\Omega,\Omega_0) = w_{\mathrm{bs},\lambda}\mathbf{r}_{\mathrm{bs},\lambda}(\Omega_0) + w_{S,\lambda}\mathbf{t}_{S,\lambda} \times \frac{\rho_{\mathrm{eff}}(\lambda)}{1-\rho_{\mathrm{eff}}(\lambda)\bullet\mathbf{r}_{S,\lambda}}\mathbf{t}_{\mathrm{bs},\lambda}(\Omega_0) \tag{3}$$

$$A_\lambda(\Omega_0) = \mathbf{r}_{\mathrm{bs},\lambda}(\Omega_0) + \mathbf{t}_{S,\lambda} \times \frac{\rho_{\mathrm{eff}}(\lambda)}{1-\rho_{\mathrm{eff}}(\lambda)\bullet\mathbf{r}_{S,\lambda}}\mathbf{t}_{\mathrm{bs},\lambda}(\Omega_0) \tag{4}$$

where $\mathbf{r}_{\mathrm{bs},\lambda}(\Omega_0)$ and $\mathbf{r}_{S,\lambda}$ are hemispherically integrated canopy reflectances, and $\mathbf{t}_{\mathrm{bs},\lambda}(\Omega_0)$ and $\mathbf{t}_{S,\lambda}$ are canopy transmittances for the black soil problem and S problem, respectively. The weight $w_{\mathrm{bs},\lambda}$ is the ratio of the HDRF for the black soil problem to $\mathbf{r}_{\mathrm{bs},\lambda}$, and $w_{S,\lambda}$ is the ratio of the canopy leaving radiance generated by anisotropic sources on the canopy bottom to $\mathbf{t}_{S,\lambda}$. The effective ground reflectance $\rho_{\mathrm{eff}}(\lambda)$ is the fraction of radiation reflected by the ground surface beneath the canopy. This variable depends on the radiation regime at the canopy bottom. Its range of variations does not exceed the range of variations of the hemispherically integrated bidirectional factor of the ground surface that is independent of vegetation [6]. Therefore, $\rho_{\mathrm{eff}}(\lambda)$ is a parameter characterizing the ground reflection. The set of various patterns of spectral effective ground reflectances is a static table of the retrieval algorithm.

B. Solutions of the Inverse Problem

A solution distribution function is introduced to provide the convergence of the algorithm [3]. The retrievals are performed

by comparing observed and modeled radiances for a suite of canopy structures and soil patterns that covers a range of expected natural conditions. The set of canopy/soil patterns, for which the magnitude of the residuals in the comparison does not exceed uncertainties in observed radiances, is used to evaluate the distribution of LAI and FPAR values, and to specify the most probable value of LAI and FPAR. Realistically, any model can only simulate a process to a certain degree of accuracy and measurements cannot be precisely made. The model predicts a domain O_S to which the "true reflectance" belongs. The same holds true for measured reflectances; that is, we can specify a neighborhood O_M around a measured reflectance in which the "true value" belongs. Any elements from these domains can be considered true values with a high probability. The neighborhoods O_M and O_S are domains of uncertainties in measurements and simulations. Domains of uncertainties depend upon the direction of direct solar radiance, view directions and the ratio of direct radiation to the total (direct and diffuse) radiation incident on the pixel. The algorithm requires not only measured canopy reflectances but also their domain of uncertainties. All canopy/soil patterns in which simulated canopy reflectances belong to the domain O_M are treated as acceptable solutions to the inverse problem. Given the set of all acceptable solutions corresponding to a measured set of spectral and multi-angle canopy reflectances $\mathbf{d}$, one counts numbers $N(\mathbf{d})$ and $N(l, \mathbf{d})$ as different values of LAI and for all solutions when LAI is less than a given value l. The solution distribution function $\Phi(l, d)$ is then defined as the ratio of $N(l, \mathbf{d})$ to $N(\mathbf{d})$, that is, $\Phi(l, \mathbf{d}) = N(l, \mathbf{d})/N(\mathbf{d})$. A precise mathematical definition of how to count "continuous" values of LAI is presented in [3]. The LAI value now can be evaluated as a weighted mean in accordance with the frequency of occurrence of a given value of l, namely

$$\mathrm{LAI}(\mathbf{d}) = \int l \, d\Phi(l, \mathbf{d}) \tag{5}$$

where the integration is performed over the interval of all possible variations of l. We note some properties of this estimation [3]. Equation (5) is sensitive to values of LAI, but not to the canopy/soil patterns generating the same LAI value. This allows the use of 3-D models of canopy structure for which a retrieved parameter may not be in the model parameter list. If the inverse problem has a unique solution for a given $\mathbf{d}$, then (5) coincides with this solution. Note that the concept of multiple acceptable solutions was originally formulated and implemented in the MISR aerosol retrieval algorithm [1], [11]. Given the solution distribution function $\Phi(l, \mathbf{d})$, one can evaluate the fraction of photosynthetically active radiation absorbed by vegetation (FPAR)

$$\mathrm{FPAR}(\mathbf{d}) = \int_{400\,\mathrm{nm}}^{700\,\mathrm{nm}} d\lambda \int \mathbf{a}_\lambda(p, \Omega_0) \, d\Phi(l, \mathbf{d}) \tag{6}$$

where $\mathbf{a}_\lambda$ is spectral canopy absorptance [3].

Concurrently, the solution of LAI is a distribution function rather than a unique value; the dispersion of LAI values can be evaluated as the root mean square deviation of the LAI solution distribution function

$$\mathrm{DLAI}(\mathbf{d}) = \left[\int (l - \mathrm{LAI}(\mathbf{d}))^2 \, d\Phi(l, \mathbf{d}) \right]^{1/2}. \tag{7}$$

In the red and near-infrared spectral space, the domain of uncertainties in measurements and simulations can be approximated by an ellipse with the major and minor axes δ_{RED} and δ_{NIR}. Consequently, the algorithm can be reformulated as the following. Given a set of spectral and simultaneous multi-angle observations of canopy reflectances $\mathbf{d}$, find all canopy/soil patterns (p represents one canopy/soil pattern), and their solution distribution functions satisfy the following inequality:

$$\frac{1}{N_{\mathrm{view}}} \sum_{v=1}^{N_{\mathrm{view}}} \left[\left(\frac{\mathbf{r}_{\mathrm{RED},v}(\Omega_v, \Omega_0, p) - d_{\mathrm{RED},v}}{\delta_{\mathrm{RED},v}} \right)^2 + \left(\frac{\mathbf{r}_{\mathrm{NIR},v}(\Omega_v, \Omega_0, p) - d_{\mathrm{NIR},v}}{\delta_{\mathrm{NIR},v}} \right)^2 \right] \leq 1 \tag{8}$$

where N_{view} is the number of view directions (nine for the MISR and up to 14 for POLDER). The values $\delta_{\mathrm{RED},v}$ and $\delta_{\mathrm{NIR},v}$ are uncertainties in measurements and simulations, are assumed known, and serve as input for the retrieval algorithm. These variables depend upon the direction of direct solar radiance, view directions, and the ratio of direct radiation to the total (direct and diffuse) radiation incident on the pixel. The MISR instrument routinely provides this information. However, the POLDER data set provides no information on the uncertainties associated with surface reflectances. Therefore, we used the following simple formula to describe the uncertainties:

$$\delta_{\mathrm{RED},v} = \delta_{\mathrm{NIR},v} = \varepsilon \left[d_{\mathrm{RED},v}^2 + d_{\mathrm{NIR},v}^2 \right]^{1/2} \tag{9}$$

where ε is the mean uncertainty assumed to remain throughout the study.

When supplied with proper data, the algorithm results in one of the following: 1) cases where no solution was found; 2) cases where solutions were found and the solution distribution function was localized to a desired value of LAI; or 3) cases where solutions were found, but there was no localization of LAI values. For the third case, the LAI values (9) are (said to be) retrieved under conditions of saturation [3]. These are important characteristics of the algorithm's behavior. We introduced indices such as the retrieval index (RI) and LAI retrieval under conditions of saturation to characterize them (discussed later).

III. Data Analysis

A. POLDER Data

The POLDER instrument is an imaging radiometer designed to provide systematic measurements of spectral, directional and polarizational characteristics of solar radiation reflected by the Earth/atmosphere system [12]. POLDER has a wide field-of-view (FOV) with a cross-track swath of 2200 km. This allows for near-complete daily coverage of the Earth surface.

TABLE I
SPECTRAL BANDS OF MISR AND POLDER INSTRUMENTS TOGETHER WITH THE CENTER WAVELENGTHS AND BANDWIDTHS

Band Name		BLUE	GREEN	RED	NIR1	NIR
MISR	Center(nm)	446	558	672	-	866
	Width(nm)	42	29	22	-	40
POLDER	Center(nm)	443	-	670	765	865
	Width(nm)	20	-	20	40	40

Every target is observed at least four times in a five day period, even at the equator. All POLDER data are geocoded, calibrated, cloud-screened, and partially corrected for atmospheric effect. POLDER products are projected on a sinusoidal equal area projection grid with a resolution of 6.17 km [13]. Detailed atmospheric correction processes are described by Leroy [14]. However, the surface reflectances were not corrected for the aerosol effects for operational reasons [15].

The spectral bands of MISR and POLDER instruments are listed in Table I. The center wavelengths of the four spectral bands of the MISR instrument are 446 nm, 558 nm, 672 nm, and 866 nm. POLDER has eight spectral bands but its current Level 2 land surface products offer four spectral bands, and the central wavelengths are 443 nm, 670 nm, 765 nm, and 865 nm, respectively. Therefore, three of the POLDER's bands designated as BLUE, RED, and NIR can be used for prototyping of the MISR LAI/FPAR algorithm. In this study, POLDER Level 2 data from November 1 through 16, 1996, over Africa and a small region of South America and Southwest Asia was used to prototype the MISR LAI/FPAR algorithm. In the algorithm, we consider the input as HDRF data, but actually, the POLDER data is BRDF measurements. Therefore, we convert BRDF to BRF and consider it as a special case of HDRF. The corresponding LUT entries are made for BRF in this case.

The maximum number of observations per pixel during this 16-day period was 14. However, due to cloud cover, the actual available data are much less and the distributions depend heavily on geolocation. The repeat observations over central Africa were often less than four, sometimes none, which is much less than in the Sahara region (over eight at least). Thus, the distribution of available POLDER data varied greatly from 0 to 14 during this 16-day period.

B. Biome Classification Map

Another important ancillary data layer used is the biome classification map (BCM), which is derived from the AVHRR Pathfinder data set [2], [16]. The BCM is a static file, i.e., it is a time-independent data set. In this map, global vegetation is classified into six biome types: grasses and cereal crops, shrubs, broadleaf crops, savanna, broadleaf forests, and needle leaf forests [16]. The distribution of POLDER data for different biomes is shown in the first row in Table II. Pixels belonging to the needle leaf forest biome attributed to only 0.25% of the total number of pixels. This biome was not considered for further analysis. In addition, only 7% of the pixels represent broadleaf forests. Note the MISR LAI/FPAR algorithm used by MISR does not use the BCM but retrieves biome types from data instead. The BCM is used for the purpose of analyzing the algorithm's behavior without being affected by biome classification process.

TABLE II
STATISTICS OF THE DISTRIBUTION OF POLDER DATA. THE FIRST TWO ROWS DENOTE THE DISTRIBUTION OF THE SIX BIOME TYPES FOR TOTAL AVAILABLE DATA AND COMPOSITED DATA. THE OTHERS INDICATE PROPORTION OF THE DATA IN THE PRINCIPAL PLANE (WITHIN $\pm 5^{\circ}$ RELATIVE AZIMUTH ANGLE) AS A FUNCTION OF BIOME TYPE AND SUN ANGLE

Biome Type		Grasses and Cereal Crops	Shrubs	Broadleaf Crops	Savanna	Broadleaf Forests	Needle Leaf Forests
Data (%)	Total	44.35	12.64	11.60	24.31	6.85	0.25
	Composite	38.68	10.31	10.36	27.43	12.99	0.23
Sun Angle (degree)		Probability in Total (%)					
10~15		0.597	0.266	0.313	0.826	0.463	-
20~25		3.677	2.664	3.214	5.581	6.128	-
30~35		1.022	0.727	1.291	1.578	2.806	-
40~45		0.131	0.228	0.073	0.035	0.003	-
50~55		0.073	0.261	0.129	0.031	0.027	-

C. Spectral Signatures

Surface information is contained within data of reflectance measurements. The amount of information that can be retrieved from data depends both on the accuracy of the data and the methods used in the retrieval process. From a spectral point of view, the intrinsic dimensionality of the remotely sensed data for a single viewing angle is determined by the number of physically independent (uncorrelated) wave bands. Instruments, such as MODIS, may contain up to seven bands of surface reflectance, and we assume useful information is stored in no more than three or four bands [17].

Spectral signatures are important sources of information. The distributions over different spectral bands for the five biomes are plotted in Fig. 1 irrespective of the viewing angles. In general, all distributions are similar in the NIR band, and in other bands, the biome spectral signatures overlap considerably. Only shrubs show a distinct distribution at RED and BLUE bands. In the RED band, grasses and broadleaf crops are similar, and likewise, savanna and broadleaf forests are similar. In the NIR band, broadleaf forests have a higher reflectance and are distinct from the others.

We plot a 25% data contour for each biome in a two-band plane to indicate where the data peak is located in order to better distinguish biome signatures (Fig. 2). A data density distribution function defined as the number of pixels per unit area in the plane was evaluated for each biome type. Each contour in this figure identifies an area of high data density that contains 25% of the pixels from a given biome type. The larger the difference between the clusters of different biomes, the better they can be distinguished in the spectral space [18], [19]. It is clear that shrubs separate well from the other biomes. In the RED-NIR plane, grasses separate from broadleaf forests. In between lay overlapping savanna and broadleaf crops. It would appear savanna, broadleaf crops and grasses would be hard to distinguish from one another if only red and near-infrared bands were used.

Although the BLUE band can be used to distinguish biomes (for example, savanna), it is currently not used in the algorithm because of large uncertainties due to strong atmosphere effects of the BLUE band data.

D. Hot Spot

The hot spot phenomenon is observed when the sun and sensor directions coincide [20]. This is a key feature of the directional signature, because its shape is sensitive to biophysical

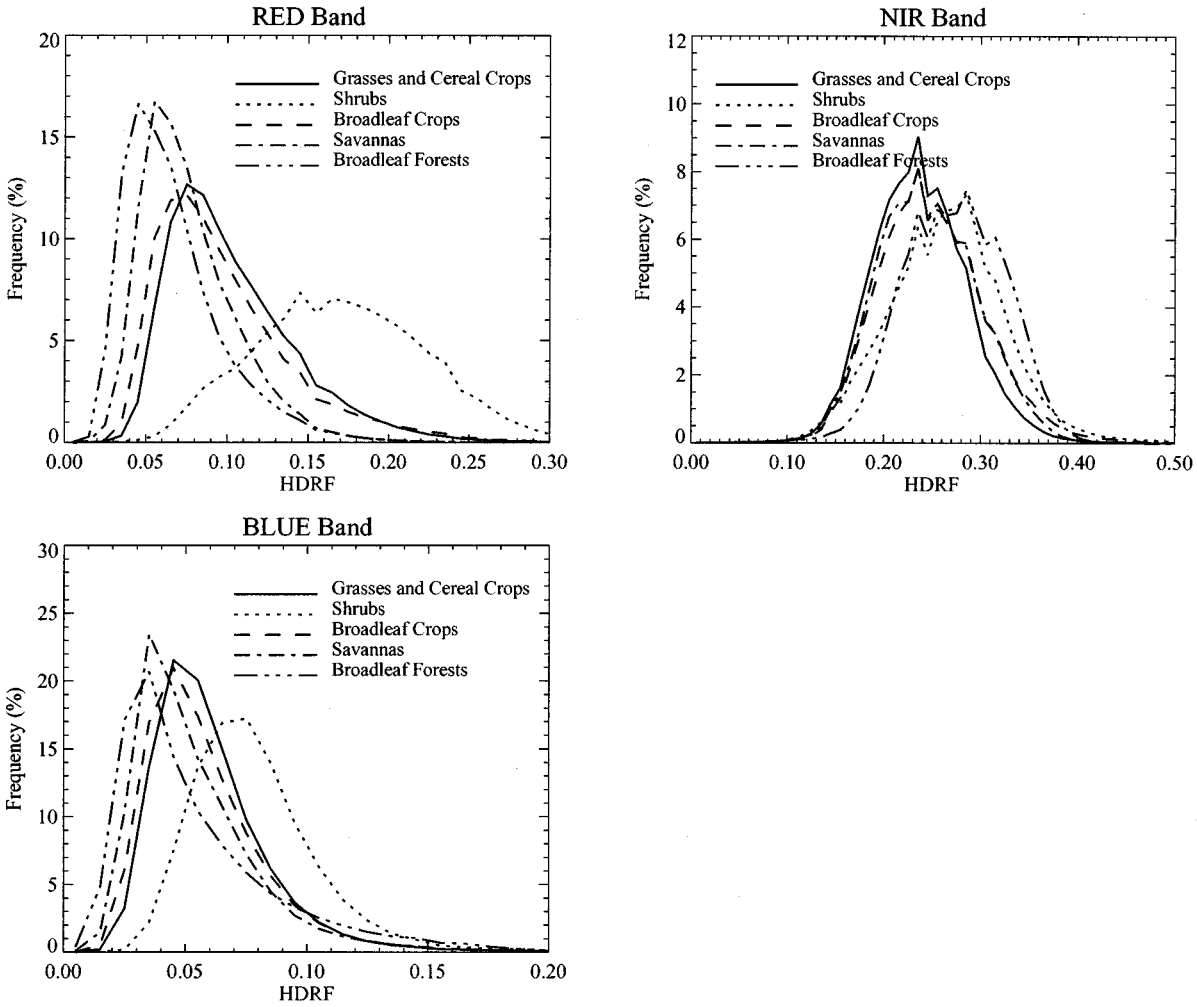

Fig. 1. Distribution of HDRF values as a function of spectral band and biome type derived from POLDER data.

parameters of vegetation such as the relative size, shape and density of the leaves [21]–[23]. The measurement of the hot spot is particularly important to multi-angle instruments [24], [25]. It is believed that directional reflectance measurements can be inverted to retrieve surface parameters such as LAI. The hot spot effect is pronounced in the visible bands, but is also obvious at all wavelengths throughout the solar spectrum. Soil conditions will also affect the hot spot effect especially in canopies that do not fully cover the surface.

POLDER data potentially provide more information by virtue of the angular signature. A drawback of POLDER for the measurement of angular signatures is its limitation to viewing angles less than 60° [12]. It is difficult to study the hot spot when the solar zenith angle is larger than 50°. Another problem in precise measurement of the hot spot signatures is the atmospheric effect on surface reflectances. Atmospheric aerosols are strongly forward scattering, which results in smoothing of the hot spot measurements [21].

The hot spot effect is best measured in the principal plane. Not all POLDER data are in the principal plane; the data nearest the principal plane (with relative azimuthal angles less than $\pm 5^{\circ}$) were plotted in Fig. 3 to show the mean angular distributions of canopy reflectances within the principal plane for different biome types, sun angles, and spectral bands. Spatial averaging was performed over all available pixels in the principal plane from each biome. However, there is not enough data for broadleaf forests at some sun angles. The curves show a clear hot spot effect at both red and near-infrared bands. For all available data, the number of pixels for which the accumulated angular reflectances about the principal plane was approximately 12.3% of the total number of available pixels. The five biomes at near-infrared have three kinds of angular signatures distinct for broadleaf forests and shrubs only. The different biomes have different reflectance magnitudes with similar shapes in the red band. Broadleaf crops and grasses/cereal crops appear similar in both bands. They are indistinguishable by their spectral and angular signatures. This can also be seen in the upper-left panel of Fig. 2.

The statistics of the angular distribution of POLDER data, i.e., the percentage of pixels with canopy angular reflectances in the principal plane over a 16-day period, are given in Table II. It is clear the data can be used to study the hot spot effect is only a small portion of the total data. For this reason, we did not consider the hot spot effect in our analysis.

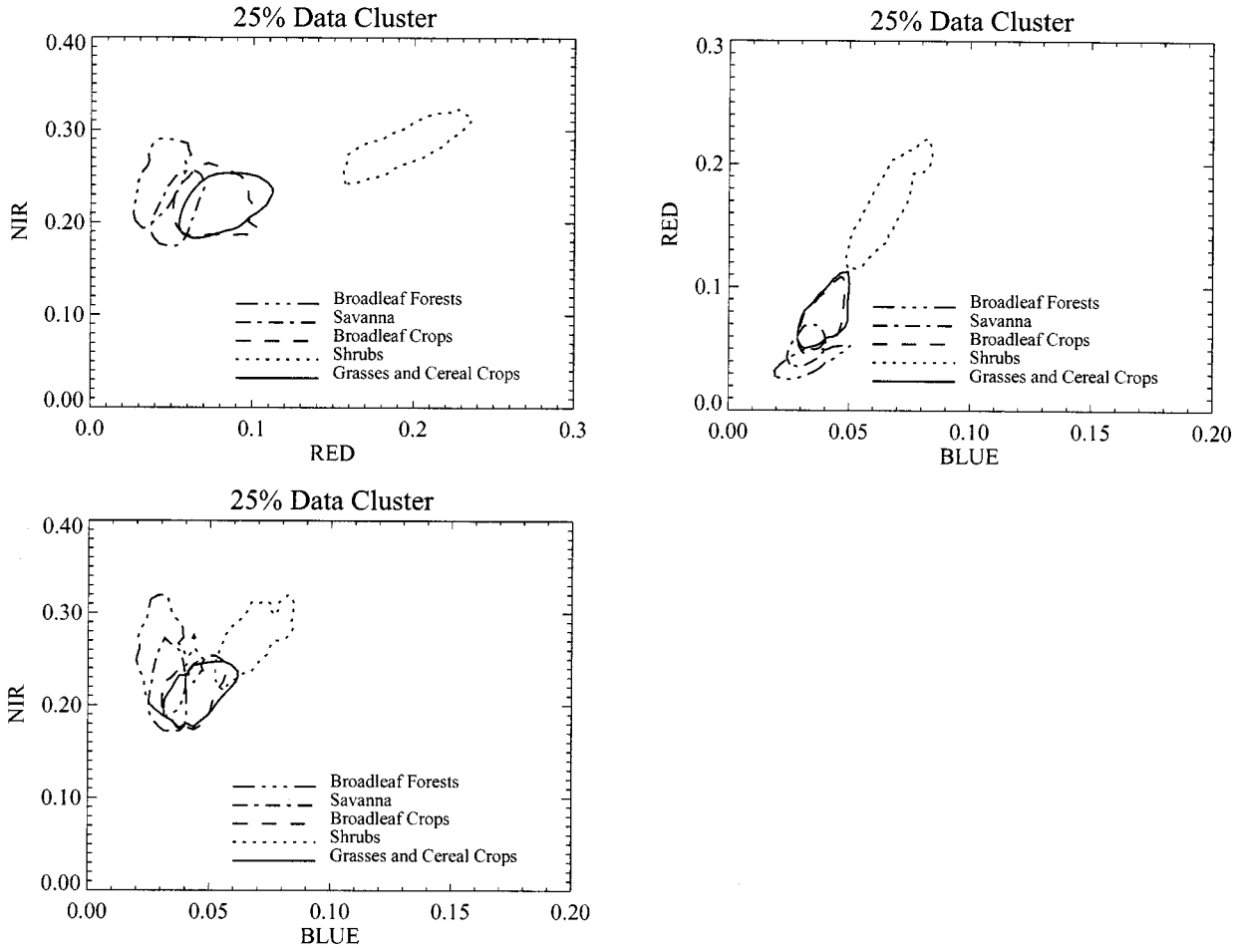

Fig. 2. Distribution of pixels from POLDER data with respect to their reflectances at two of the three available wavelengths. Each biome-dependent contour separates a set of pixels representing the most probable patterns of canopy structure from a given biome type.

IV. Prototyping Results

The MISR instrument will provide HDRF and BHR measurements along with their uncertainties [1], [2], [26]. The LAI/FPAR algorithm is designed to utilize this information in a two-step process. The first step uses BHR measurements to identify canopy/soil patterns that are acceptable solutions. Then, the HDRF test is used as a more stringent test to select canopy/soils patterns from the previous set. The most probable value is then specified. However, the POLDER instrument does not provide BHR's. Therefore, we skip the first step and directly use the HDRF test to prototype the MISR LAI/FPAR algorithm for results.

For the purpose of using POLDER data to prototype the algorithm, the following three cases with only the HDRF test were performed: 1) using one view angle, the near-nadir view; 2) using multi-angle data, that is, six angles from all available directions; and 3) using all available multi-angle data (about 12 or more directions).

To minimize uncertainties in the POLDER data, we composite 16-day POLDER data into one layer using a maximum near-nadir NDVI method similar to the maximum value compositing (MVC) technique used by James and Kalluri [27]. Since surface anisotropic properties will affect the measurements, nadir or near-nadir reflectance is the preferred choice. The nadir pixels have the finest spatial resolution with minimal distortion, and atmospheric correction is most reliable and accurate for near-nadir measurements. A threshold NDVI value of 0.1 was used to ensure that the pixel is vegetated in certain cases. The distribution of the composited POLDER data for different biomes is illustrated in Table II.

A. Retrieval Index

A pixel for which the algorithm retrieves a value of LAI and FPAR is termed a successful pixel (a successfully retrieved pixel). A pixel for which no solution was found is termed an unsuccessful pixel (an unsuccessfully retrieved pixel). The ratio of the number of successful to total number of pixels is defined as the retrieval index (RI)

$$\mathrm{RI} = \frac{\text{successful pixels}}{\text{total number of pixels}} \cdot 100\%. \tag{10}$$

The RI is a simple indicator of the behavior of the algorithm. It demonstrates the percentage of pixels with successful retrievals for a data set by the algorithm.

The RI increases with increases in mean uncertainty ε (9). However, the quality of retrieved LAI/FPAR fields decreases with an increase in ε; it allows for a wider set of acceptable

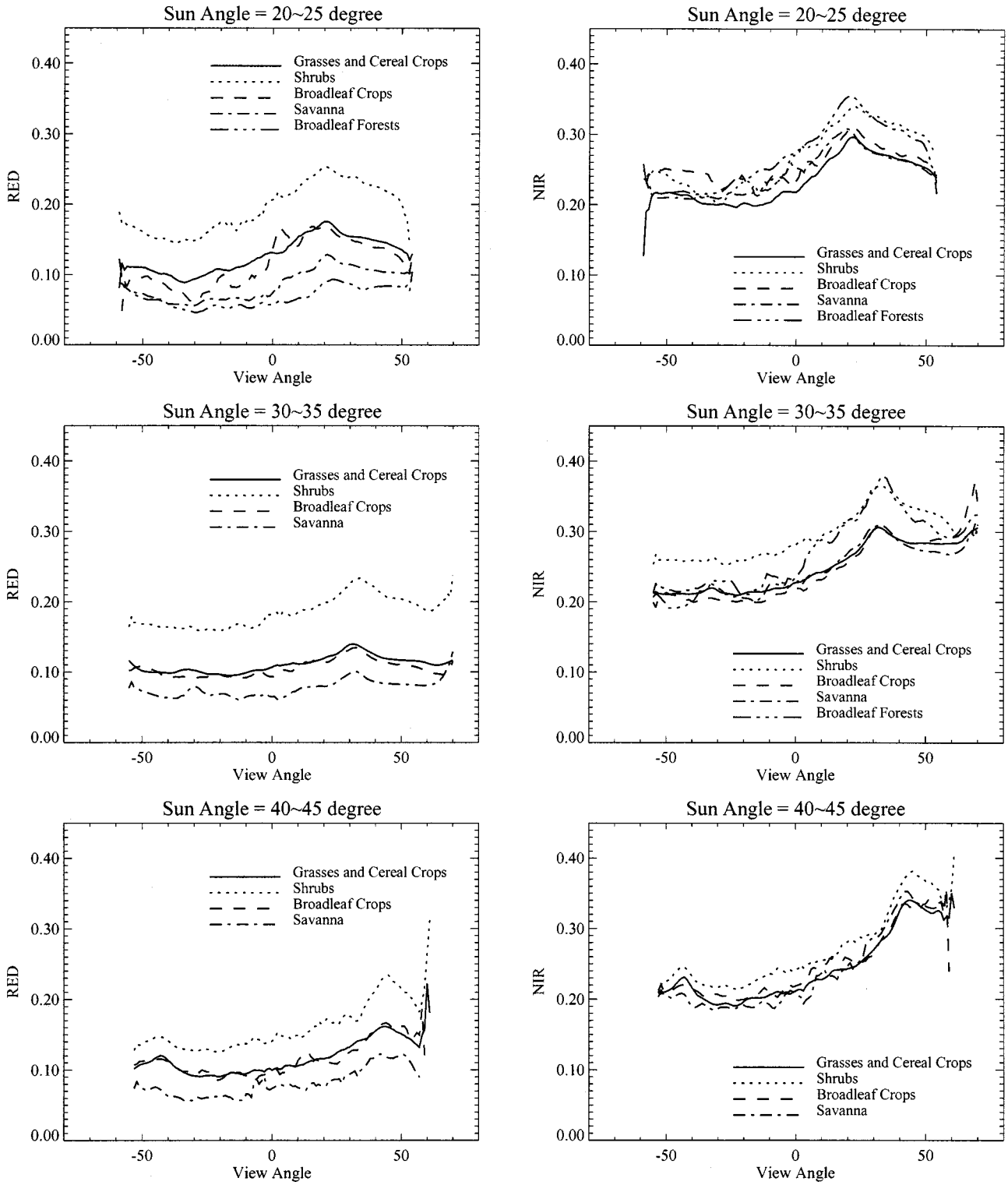

Fig. 3. Angular signatures of averaged HDRF's of POLDER data in the principal plane (within $\pm 5^{\circ}$ relative azimuth angle) as a function of biome type at different sun angles. Some of the curves of broadleaf forests are missing because of insufficient data.

solutions. If ε is underestimated, the algorithm fails when real uncertainties in surface reflectances are greater than those determined by (9). However, if ε is overestimated, the algorithm produces a wider set of acceptable solutions. Therefore, there is a critical value of ε for which (9) optimally approximates real uncertainties. According to our experience, a ε of 0.2 is a good approximation [10]. Since uncertainties were unknown for POLDER data. The actual uncertainties depend on the spectral band and direction of view. The uncertainties of retrieved surface reflectances are usually higher at shorter wavelengths and larger view zenith angles due to atmosphere effects. Therefore, the use of mean uncertainty ε in (9) is a compromise. MISR of-

TABLE III
RETRIEVE INDEX AND FREQUENCY OF LAI UNDER SATURATION FOR SIX BIOMES AT MEAN UNCERTAINTY $\varepsilon = 0.2$

($\varepsilon = 0.2$) (%)	No. of View Angle	BCM Biome Type				
		Grasses and Cereal Crops	Shrubs	Broadleaf Crops	Savanna	Broadleaf Forests
Retrieval Index	1	99.5	99.9	99.2	98.1	40.6
	6	84.0	80.8	73.4	74.9	18.9
	12	80.8	79.3	68.4	72.3	18.4
LAI Saturation Frequency	1	0.01	0.02	6.26	9.76	30.1
	6	0.0	0.01	2.52	6.18	17.4
	12	0.0	0.01	2.37	5.69	15.9

fers HDRF, BHR, and their uncertainties as functions of spectral bands and viewing angles. The algorithm is expected to give better results after utilizing the advantages of these inputs.

The retrieval indices that in single- and multi-angle cases for six biomes at $\varepsilon = 0.2$, are shown in Table III. It demonstrates that RI decreases with the use of more view angles. This is expected because the uncertainties of distributed view-angles are often larger than a direction near the nadir, and multi-angle data generally have higher uncertainties than single-angle data. If the uncertainties between the two are comparable, the mutli-angle test based on angular dependent information is a more stringent test than the single-angle test.

The retrieval indices for corresponding multi-angle retrievals are low, indicating that multi-angle data have larger uncertainties at off-nadir directions. It could also imply that the pre-assigned biome type is incorrect, as it is possible that the multi-angle test distinguishs biomes when the single-angle test cannot. It may also imply that the limited number of canopy structural types (six biomes) used by the algorithm does not represent all the canopy types encountered in reality. Mixtures of more than one biome types will blur the architectural distinctions and the canopy reflectance of mixed patterns may be different from those of pure biomes. In addition, it may indicate that low resolution data result in smoothing canopy reflectance features, especially in the case of mixed stands [28]. This may be one of the important limitations of prototyping the algorithm on coarse resolution data. Finally, it is also possible that failures may result from the data quality. For example, if the canopy reflectances are retrieved with high uncertainties in the process of atmospheric correction.

When using the RI metric to evaluate LAI/FPAR retrievals, one should remember that a higher RI does not necessarily denote that the retrieved LAI and FPAR fields are correct or accurate, and the mean uncertainty ε is not a sufficient criterion and individual uncertainties with input data and models should be considered.

B. NDVI Distributions of Successful and Unsuccessful Pixels

The characteristics of successful and unsuccessful pixels provide information on where and why the algorithm failed. The NDVI histograms of successful and unsuccessful pixels for an $\varepsilon = 0.2$ are demonstrated in Fig. 4. The distribution of NDVI values of successful pixels is slightly dependent upon the number of view angles used. The NDVI distribution of successful pixels is close to the actual NDVI distribution of the data set because retrieval indices were high for all biomes ($\mathrm{RI} > 70\%$), with the exception of broadleaf forests. Amongst the six biomes, shrubs and broadleaf forests exhibit distinct patterns. Successful pixels of shrubs are mainly characterized by low values of NDVI in contrast to broadleaf forests.

The unsuccessful pixels causes the shape of the NDVI distribution to vary with the number of view angles. However, the number of unsuccessful pixels for the single-angle case is a small fraction of the total number of pixels for all biomes ($\mathrm{RI} > 98\%$) except in the case of broadleaf forests. Most of the biomes, except shrubs, generally show unsuccessful retrievals at high NDVI values (0.5 to 0.8). High NDVI values indicate dense canopies, where about 80–95% of radiation at the red spectral band is absorbed. The canopy reflectances at this wavelength are very low and uncertainties may exceed the threshold value of mean uncertainty ($\varepsilon = 0.2$). Note, however, the most probable NDVI values of successful and unsuccessful pixels for broadleaf forests are 0.85 and 0.7, respectively. Canopy structure can vary considerably when NDVI is unchanged [10]. Therefore, this feature of NDVI distribution indicates the algorithm is sensitive to canopy structure, but not to the magnitude of NDVI.

C. LAI under Conditions of Saturation

In the case of a dense canopy, reflectance can be insensitive to the parameters in cerain directions. The canopy reflectance is then said to belong to the saturation domain [3]. Therefore, the reliability of parameters retrieved under conditions of saturation is very low. In other words, the retrieved solution distribution function does not localize LAI values.

The frequency of LAI under saturation increases with increasing uncertainties when more pixels are included in the category of successful pixels and more realizations are included in the solution distribution. For a fixed mean uncertainty ($\varepsilon = 0.2$), the LAI saturation frequency decreases with an increase in the number of view angles (Table III). This is a desirable attribute of the algorithm, because it leads to a decrease in the dispersion of LAI values or the retrieval uncertainty of LAI values. This is important evidence that multi-angle data contain more information, and is utilized by the algorithm to reduce saturation and localization of the LAI value. Ascertaining if the solution distribution function belongs to the saturation domain is a special feature of the dispersion of LAI values (discussed in detail later). This has been previously formulated in [3]. The saturation conditions are quite different for the six biomes. Grasses and shrubs have nearly no saturation and broadleaf forests have the highest saturation frequencies, as expected. The frequency of LAI values retrieved under conditions of saturation in the case of single-angle high resolution data, such as TM data (30 m resolution) [10], is approximately the same for low resolution single-angle near-nadir POLDER data. Therefore, the information content of multi-angle data at coarse resolution may be comparable to that of single-angle high resolution data. This is one confirmation of the validity of the theorem cited in Section II-A, because the inverse problem has a unique solution. The problem of "saturation" does not exist for "ideal" multi-angle data. Therefore, inclusion of more angular information tends to eliminate this problem.

The results presented thus far showcase a benefit of multi-angle data over single-angle data, but also that there is no significant benefit of using 12 angles compared to six angles in our analysis. This is because the MISR look-up table (LUT) was

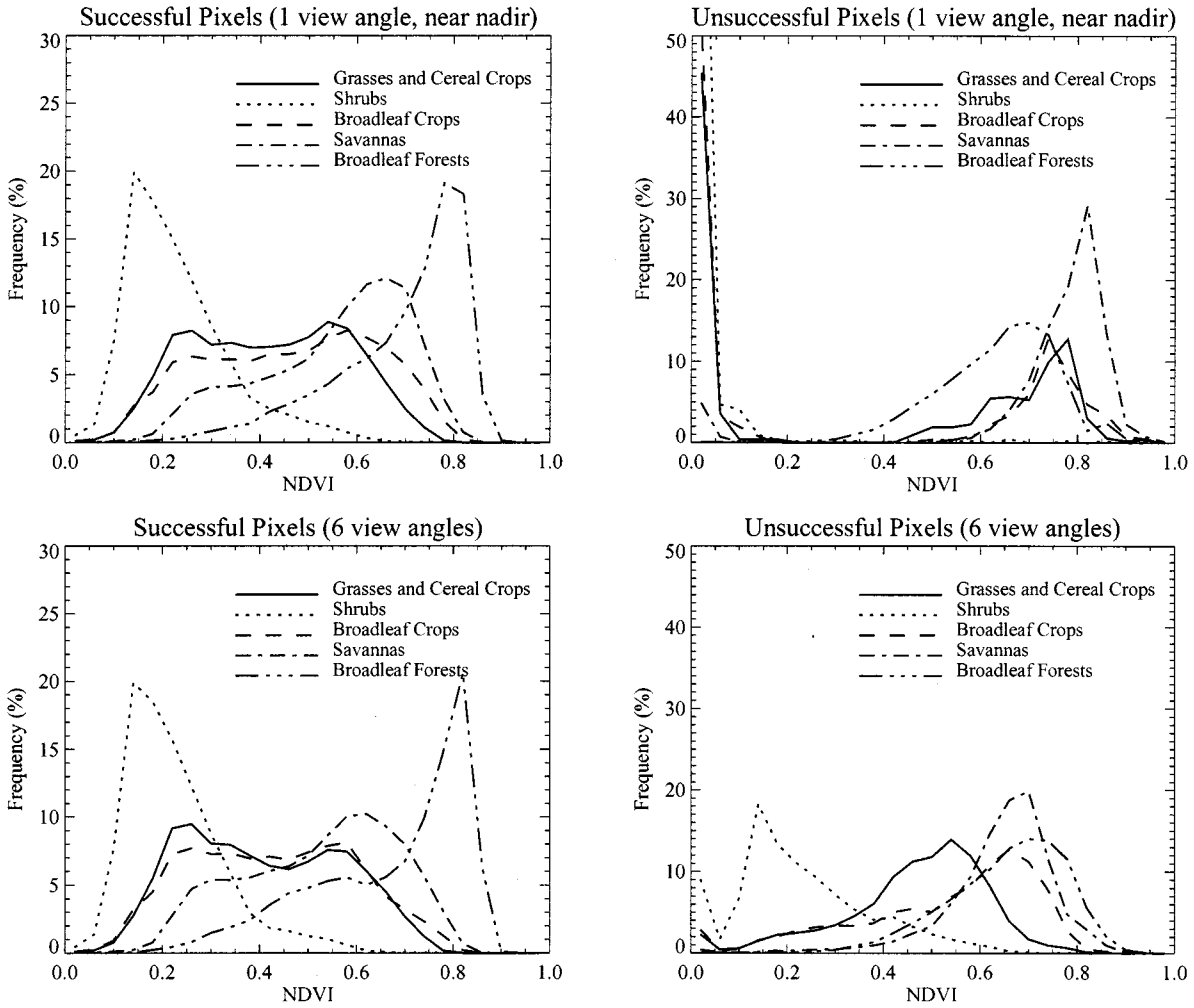

Fig. 4. NDVI histograms for five biomes in the single-angle case and multi-angle case. The left column of two panels shows the distribution of successful pixels with respect to their NDVI values. The right column shows the distribution of unsuccessful pixels.

designed to distinguish five intervals in view zenith angles (i.e., ten directions in one azimuthal plane). The 12 POLDER view directions were distributed amongst them. Therefore, the algorithm is sensitive to six view directions but only slightly to 12 view directions. In addition, the use of more directions increases not only the information content but also their uncertainties.

The dispersion of retrieved LAI values is closely related to the saturation domain. The saturation domain is a special case when the measured data are slightly influenced by canopy structure and the dispersions are very large. Thus, the dispersion of LAI acts as an indicator of the quality of LAI retrieval. The dependence of dispersion on the most probable value of LAI shows that increases in the magnitude of LAI tends to increase the dispersion of its retrieval (Fig. 5). However, the inclusion of more angular information results in decreased values of the dispersion. This corresponds to better localization of the LAI distribution function and a higher accuracy of estimated LAI values. This is an additional evidence of the benefit of multi-angle data. The histogram of the retrieved LAI field is a statistical characteristic of the retrieved parameter. The histograms of retrieved LAI values as a function of the number of view angles for the five biomes are shown in left panels of Fig. 6. The last panel in this figure shows the ten-year average LAI histograms derived from the AVHRR Pathfinder data by Myneni *et al.* [16]. This comparison is valuable in that it helps us to indicate if the algorithm catches the general LAI distribution patterns for different biomes.

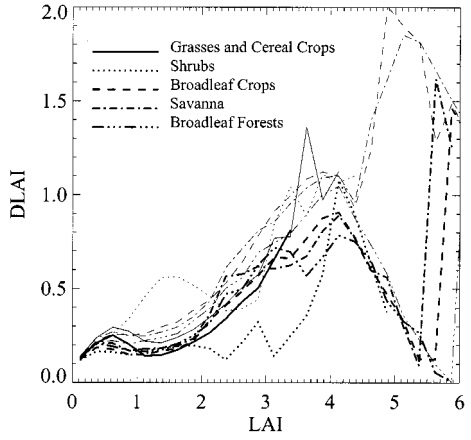

Fig. 5. The relationships between dispersion of LAI and LAI values for the single-angle case (thin line) and multi-angle case (thick line). The relationships are calculated by averaging dispersion of LAI over a small interval of LAI values.

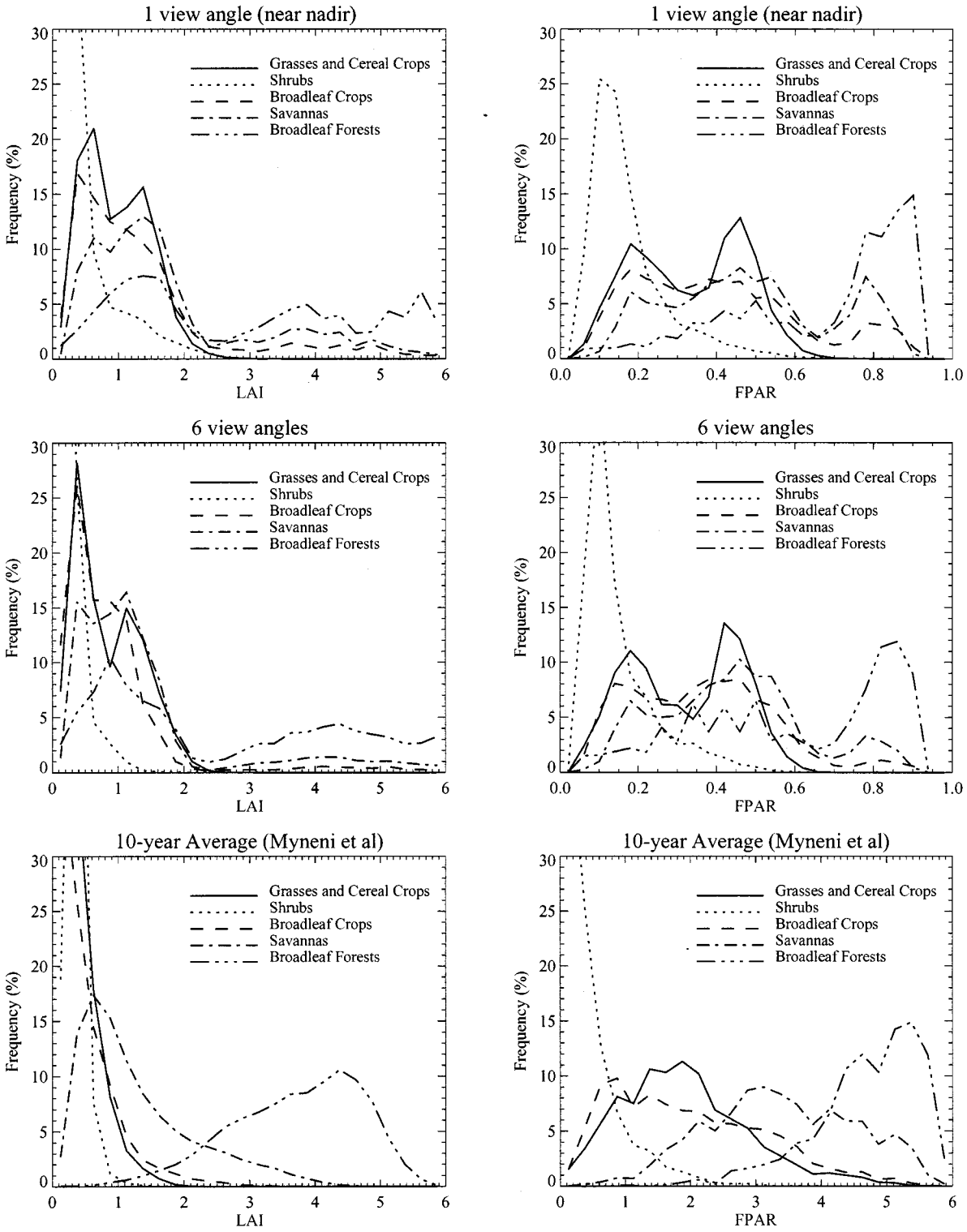

Fig. 6. Histogram of retrieved LAI and FPAR for the sigle- and multi-angle data cases and from a ten-year average derived from AVHRR Pathfinder data [16].

D. Histograms of LAI and FPAR

The majority of retrieved LAI values are less than 2.5; broadleaf crops, savanna and broadleaf forests generally have higher LAI values. Shrubs and broadleaf forests are distinct in their LAI distributions. In the case of multi-angle data, the retrieved LAI values are somewhat smaller for all biomes but distributions are similar. Note, high LAI values correspond to low values of red reflectance and to high uncertainties. Therefore, many of the pixels with possibly high LAI cannot be retrieved. This implies that i nformation about uncertainties is also very important in order to improve the performance of the algorithm, as discussed in Section IV.A. In comparison to the result from the AVHRR data, the distributions for shrubs

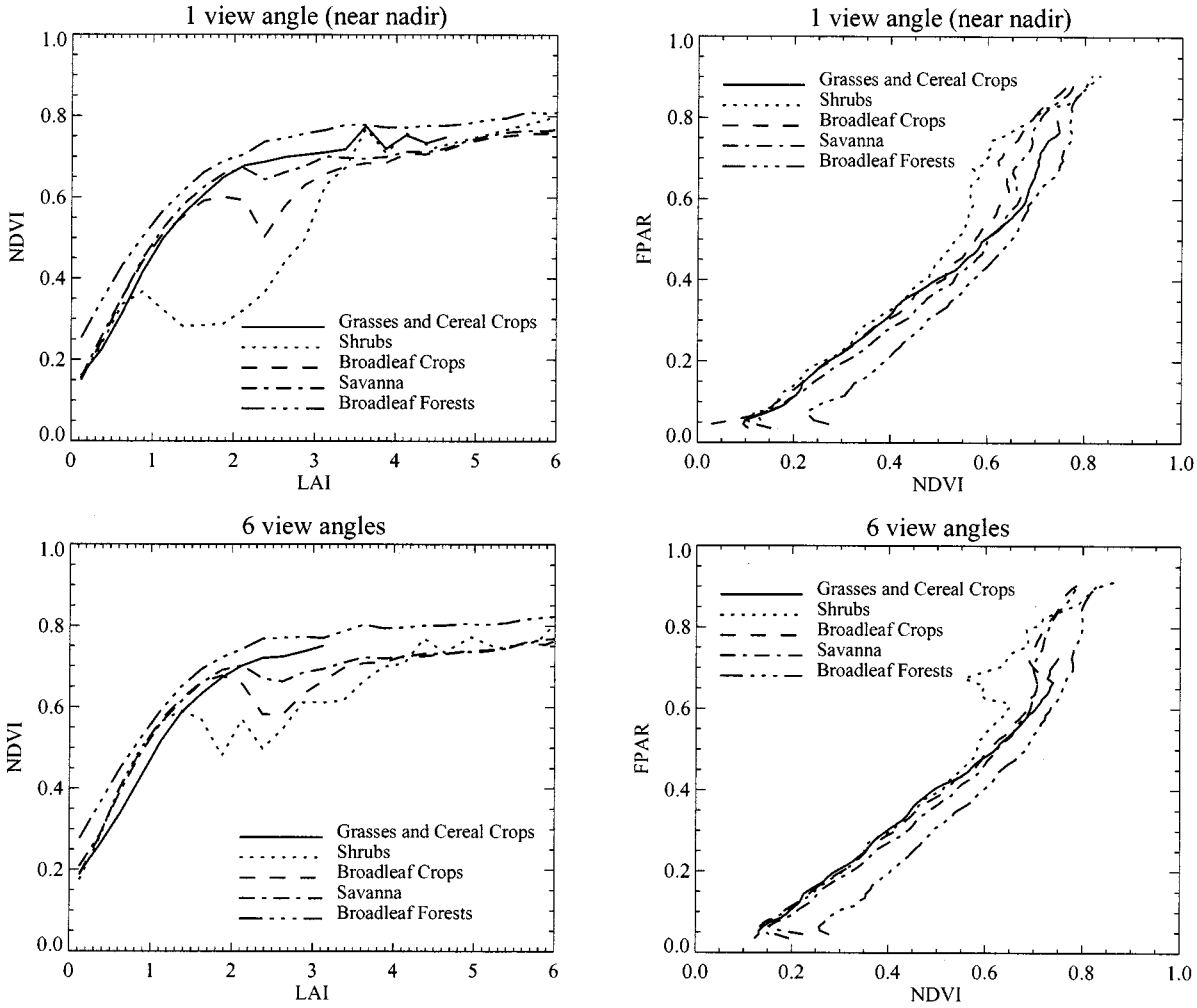

Fig. 7. Average NDVI-LAI and NDVI-FPAR relationships for single- and multi-angle cases. The left column is NDVI-LAI relationship in the single-angle and multi-angle cases, and the right column is the NDVI-FPAR relationship.

and savanna seem to match well. Grasses and broadleaf crops also show comparable tendencies. Broadleaf forests have an anomalously higher frequency at the low end of LAI. A detailed analysis of broadleaf forests will be presented later.

The right panels in the Fig. 6 are the cases of single- and multi-angle data retrievals and the ten-year average from the AVHRR data for FPAR histograms. The histograms of FPAR for different biomes match well with ten-year averages. When comparing single-angle and multi-angle results, one can detect the frequency of high FPAR values decreases slightly with decreasing number of observations. This corresponds to high NDVI values.

E. NDVI-LAI and NDVI-FPAR Relationships

The relationships between a spectral vegetation index such as NDVI and surface biophysical variables LAI and FPAR have been studied extensively [29]–[31]. Their relationships are often used as an empirical, but effective way of calculating LAI and FPAR [16], [17], [32]–[34]. These products will likely be used in biophysical and biogeochemical models by potential users. This demands the retrieved LAI and FPAR fields possess the same statistical properties as those derived from ground based measurements. Therefore, NDVI-LAI and NDVI-FPAR regression curves using retrieved LAI and FPAR fields and near-nadir NDVI derived from POLDER data were calculated (Fig. 7). The left column of panels in Fig. 7 shows the relationships of NDVI and LAI retrieved from single-angle and multi-angle observations, respectively. The right column shows the relationships of NDVI to FPAR. These relationships generally correspond to those reported in the literature [16], [32]. However, their forms vary with biome types and this is not clearly seen here. This is the effect of resolution will be discussed in a later section.

It is known that the NDVI-LAI relationship is an increasing function with a shape determined by biome type. The problem with shrubs is worthy of notice. It is obvious that the NDVI-LAI relation is poorly estimated with shrubs using single-angle data. However, the use of multi-angle data greatly improves it (Fig. 7). Shrubs are a special biome type characterized by extreme lateral heterogeneity with low to intermediate vegetation ground cover (0.2–0.6), small leaves, woody material, and bright soil backgrounds [16]. Shrubs are the most discontinuous of all biome types, and the radiation regime is greatly influenced by soil background. For a single-angle near-nadir view, the influence

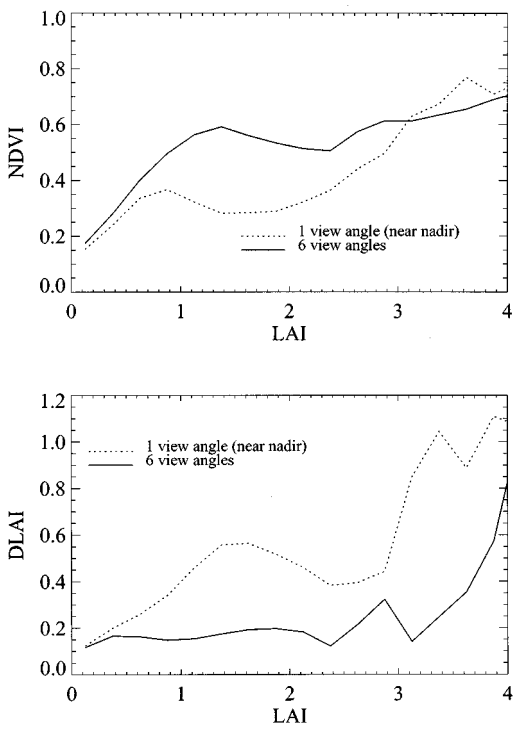

Fig. 8. The average NDVI-LAI relationship of shrubs and the corresponding LAI-DLAI relationship in the single-angle and multi-angle cases.

of soil is dominant and can lead to incorrect retrievals. Multi-angle data contains more information and hence retrievals are superior. This is illustrated in Fig. 8. For an LAI range of approximately 1.0 to 3.0, the single-angle NDVI-LAI relation is greatly distorted, and the dispersion of retrieved LAI can be as high as 0.5. The LAI dispersion then decreases dramatically for multi-angle retrievals.

Although the NDVI-LAI relationship of shrubs includes high LAI values, only 1.6% of the pixels have a LAI greater than 2.0, and 13% of the pixels have a LAI larger than 1.0. The relationship at high LAI values is based on little data. The same case exist with respect to the NDVI-FPAR relationship. Generally, it is a near-linear relation. Also note that the range of variation in LAI values for grasses is reduced from $[0, 5]$ for the single-angle case to $[0, 3]$ for the multi-angle case.

F. Biome Classification

Biome classification derived from multi-view angle data is an additional goal of the MISR LAI/FPAR algorithm. This goal is based on an assumption that multi-angle data contain more information about vegetation canopy structure, and can be exploited to obtain biome information along with LAI and FPAR. The algorithm estimates both the expected LAI value and its dispersion according to the solution distribution function. It is possible, in principle, to utilize this dispersion to identify biome type. The procedure is the same as in [2]. The algorithm is executed for each pixel five times using the five biome look-up tables (LUT's). Assuming that at least one of the candidate biomes passes the HDRF test, the biome with minimum LAI dispersion is chosen. If the same minimum value is found for more than one biome, the biome with the smallest LAI is chosen. However, if this process fails to identify a unique biome type, the algorithm is deemed unsuccessful. A biome classification map denoted as the MISR biome classification map (MBCM) is derived.

TABLE IV
BIOME TYPE DISAGREEMENT AND MISVALUATION MATRIX BETWEEN THE BIOME CLASSIFICATION MAP (BCM) DERIVED FROM THE AVHRR DATA AND MISR BIOME CLASSIFICATION MAP (MBCM). THE DIAGONAL ENTRIES IN THE FIRST SUB-ROWS (MARKED A FOR AGREEMENT) SHOW THE PERCENTAGE OF DATA WITH AGREED BIOME TYPE ASSIGNED BY MBCM AND BCM. THE OTHER ENTRIES IN THE FIRST SUB-ROWS SHOW THE PROPORTION OF PIXELS IDENTIFIED AS OTHER BIOMES SPECIFIED BY MBCM. THE DIAGONAL ENTRIES IN THE SECOND SUB-ROWS (MARKED E FOR EVALUATION) SHOW THE PERCENTAGE OF DATA IS EVALUATED REGARDLESS OF THE BIOME TYPE IN MBCM. THE OTHER ENTRIES SHOW THE PROPORTION OF PIXELS CLASSIFIED INTO OTHER BIOME TYPES BY MBCM AND THOSE RESULTING IN AN INCORRECT ESTIMATION OF LAI

			MBCM Biome Type				
		(%)	Grasses and Cereal Crops	Shrubs	Broadleaf Crops	Savanna	Broadleaf Forests
BCM Biome Type	Grasses and Cereal Crops	A	21.21	12.66	5.02	22.13	38.98
		E	49.23	5.64	2.04	8.67	34.42
	Shrubs	A	13.56	9.91	1.80	48.09	26.64
		E	4.81	73.85	0.10	0.17	21.07
	Broadleaf Crops	A	24.49	14.50	5.87	24.42	30.72
		E	18.06	0.50	57.33	1.34	22.77
	Savanna	A	31.21	17.32	7.38	17.48	26.61
		E	22.26	0.98	0.04	57.18	19.54
	Broadleaf Forests	A	32.99	22.95	11.09	23.24	9.73
		E	29.97	21.83	8.46	21.95	17.79

Table IV summarizes disagreement between the biome map derived from the MISR algorithm (MBCM) and the map described in Section III.B derived from the AVHRR data (BCM). The table is a five by five matrix with BCM biome types in rows and MBCM biome types in columns. The ratio of pixels belonging to agreement of two maps to all pixels for each of the BCM biome types is given together with the rate of disagreement. If the two LAI retrievals for a pixel, based on BCM and MBCM, are within 20%, the LAI of the pixel is assumed correctly evaluated even if the assigned biome types are different. Then, the rate of misevaluation is defined as the ratio of pixels in disagreement and have differences larger than 20% in retrieved LAI's to all pixels. The two sub-rows in Table IV, marked "A" and "E", show the rates of biome type agreement (the diagonal entries) and biome type disagreement (other entries), and the rates of correct LAI evaluation (the diagonal entries) and misevaluation (other entries), respectively.

It is clearly shown that the disagreement rate is rather high and all biomes have very low agreement rates. For diagonal entries, the evaluation rate is always larger than the agreement rate and for other entries, the misevaluation rate is always less than the disagreement rate. It is clear that disagreement of the biome type by the algorithm does not necessarily lead to misevaluation. It should be recalled the distribution of grasses and broadleaf crop pixels in the red and near-infrared space were similar (Fig. 2). The NDVI-LAI relationships were also similar at low LAI values (Fig. 7). Therefore, a biome type disagreement in this case does not result in poor LAI retrievals. Figs. 5 and 6 can help us understand this concept. Variations in biome specific dispersions are small at low values of most probable LAI's. Therefore, they are indistinguishable with respect to the dispersion for LAI values from the interval $[0, 1.75]$. A total number of pixels whose LAI values belong to this interval make up 88% according to the BCM and 87% according to the MBCM. It

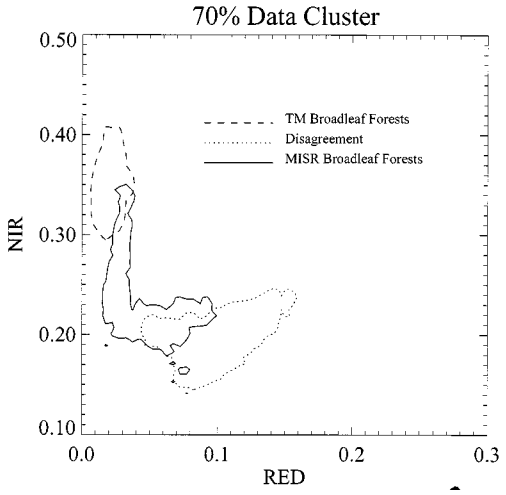

Fig. 9. Distribution of pixels for MBCM and BCM agreed as broadleaf forests, and disagreement of MBCM with broadleaf forests from BCM of POLDER data and broadleaf forests of TM data. Each contour shows the highest data density area, which contains 70% of the pixels for a given dataset.

means that the biome types for most pixels cannot be identified; however, it does not lead to misevaluation of LAI values. The evaluation rate given in Table IV is also influenced by the RI. For broadleaf forests, the evaluation rate is 17.8%, and the RI is also low: 18.9%. This shows a very high percentage of correct evaluation.

Disagreement of the biome type from the algorithm could be due to many reasons. First, characterization of global vegetation as six biomes is probably not an adequate representation of all situations encountered in reality. A typical problem is biome mixtures. Second, low spatial resolution of the data smoothes structural features of vegetation. Also, biome mixture increases with decreasing spatial resolution. In POLDER data, the biomes overlap considerably in spectral space, especially grasses, broadleaf crops and savanna (Fig. 2). The biomes separate better with high resolution data such as thematic mapper (TM) data because the pixels are likely to contain mostly one biome type. Therefore, the low resolution of POLDER data smooths some of the architectural features of the biome types and this leads to disagreement.

Fig. 9 shows distribution of broadleaf forest pixels in the red and near-infrared spectral space. The contour labeled "MISR Broadleaf Forests" contains pixels identified in BCM and MBCM as broadleaf forests. The contour "TM Broadleaf Forests" was derived from Landsat TM Data using a ground-based map [10]. The third contour, "Disagreement," depicts pixels marked in BCM as broadleaf forests and identified by the MISR algorithm as nonbroadleaf forests. One can see the contours TM Broadleaf Forests and MISR Broadleaf Forests tend to occupy similiar space. The red reflectances of pixels in Disagreement varies between 0.05 and 0.15. This indicates the presence of soil or nongreen material contributions. This conflicts with the definition of broadleaf forests. This example demonstrates the ability of the MISR algorithm to identify the correct biome types even when the full complement of information (e.g., uncertainties, BHR's) is not available.

TABLE V
ROOT MEAN SQUARE ERROR (RMSE) OF BHR EVALUATION AT TWO SPECTRAL BANDS IN THE CASE OF GRASSES AND CEREAL CROPS. THE LUT TEST INDICATES USE OF LUT ENTRIES PLUS NOISE AS HDRF INPUTS, AND MODEL TEST INDICATES USE OF SIMULATED HDRF'S AND BHRS BY A CANOPY RADIATION MODEL

RMSE(%)	LUT Test						Model
(noise)	0%	5%	10%	15%	20%	25%	Test
RED	0	2.47	3.94	5.55	6.88	8.16	8.51
NIR	0	1.37	2.22	3.18	4.14	5.21	4.78

TABLE VI
INPUT PARAMETERS FOR THE DISCRETE ORDINATES RADIATIVE TRANSFER CODE [20] TO SIMULATE BHR AND HDRF IN THE CASE OF GRASSES AND CEREAL CROPS

LAI	0.5	1.0	1.5	2.0	3.0	5.0
Sun Zenith Angle (deg)	1.0	15.0		30.0	45.0	60.0
View Zenith Angle (deg)		0 ~ 60		Randomly selected		
View Azimuth Angle (deg)		0 ~ 60		Randomly selected		
Reflectance (%)			11.64			42.71
Transmittance (%)	RED		11.24		NIR	47.90
Soil Reflectance (%) - Medium			11.20			13.20

It was noted previously that the NDVI-LAI relations of different biomes were similar (Fig. 7). This may be attributed to the low spatial resolution of the data, which leads to the biome type disagreement. MISR data is expected to be better for biome classification because it has better atmospheric correction. This implies smaller reflectance uncertainties, wider angular coverage (up to 70°), which implies more information, and smaller pixels (1.1 km), which implies less mixed biomes.

V. EVALUATION OF BHRS FROM POLDER DERIVED HDRF DATA

A. Methodology

As mentioned previously in Section IV, the MISR LAI/FPAR algorithm has two tests—BHR and HDRF test, which utilize the full information content and uncertainties from the MISR instrument in the process of information extraction. Data from POLDER consist of BRDF measurements only [14], [15]. As mentioned before, BRDF can be converted to BRF and used in replace of HDRF. Therefore, a "shared version" of the algorithm was used to produce the LAI-FPAR fields. This shared version allows the evaluation of BHR's. The aim of this section is to describe a method to evaluate an accurate BHR from multi-angle data.

Based on (3)–(4), we can relate BHR $[A_\lambda(\Omega_0)]$ and HDRF $[\mathbf{r}_\lambda(\Omega,\Omega_0)]$ by

$$\mathbf{r}_\lambda(\Omega,\Omega_0) = w_{\mathrm{bs},\lambda}\mathbf{r}_{\mathrm{bs},\lambda}(\Omega_0) + w_{S,\lambda}[A_\lambda(\Omega_0) - \mathbf{r}_{\mathrm{bs},\lambda}(\Omega_0)]. \quad (11)$$

In this equation, the term with the effective ground reflectance $\rho_{\mathrm{eff}}(\lambda)$ disappears. If the correct value of BHR is known, the HDRF can be evaluated without knowledge of ground reflectances. The LAI retrieval problem based on POLDER

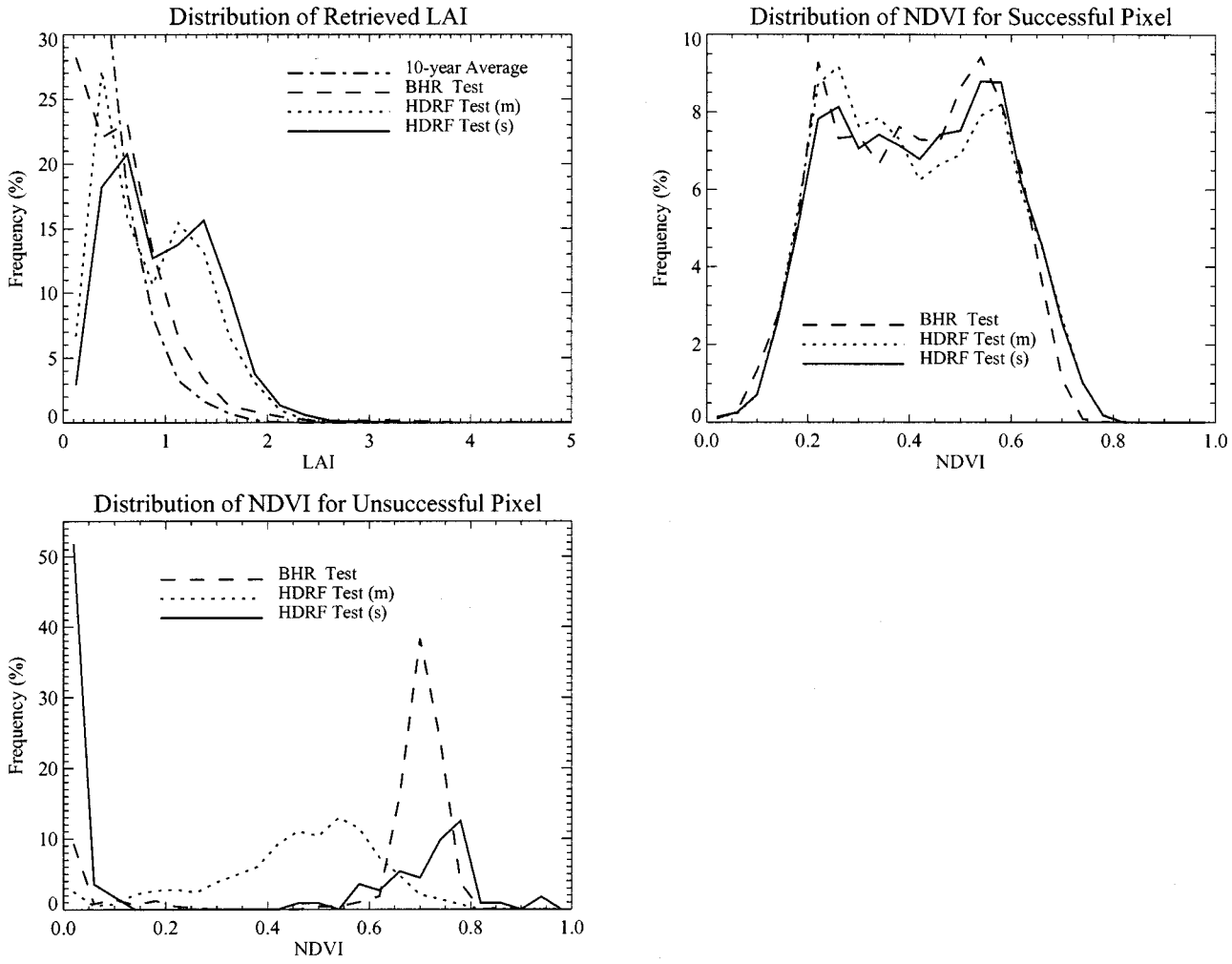

Fig. 10. Grasses and cereal crops data from the biome classification map (BCM) used as input for three different tests: the single-angle HDRF test, the multi-angle HDRF test, and the BHR test. The upper-left panel shows the distribution of retrieved LAI in the three cases and one from the ten-year average LAI distribution over Africa for the same time period and same biome type [16]. The upper-right panel shows the distribution of NDVI from successful pixels. The lower-left panel shows the distribution of NDVI from unsuccessful pixels. In this figure, (s) indicates near-nadir direction HDRF only, and (m) indicates multidirection HDRF data.

data can be reformulated as follows. Given $r_{\lambda,\mathrm{mes}}(\Omega)$, find such A_λ and the solution distribution function $\Phi(\mathrm{LAI}, A_\lambda)$ that minimize the following function

$$\sum_{k=1}^{N} \int [r_{\lambda,\mathrm{mes}}(\Omega_k) - r_\lambda(\Omega_k, A_\lambda)]^2 \, d\Phi(\mathrm{LAI}, A_\lambda) \qquad (12)$$

where $r_{\lambda,\mathrm{mes}}(\Omega_k)$ are the HDRF measurements. $r_{\lambda,\mathrm{mod}}(\Omega_k, A_\lambda)$ equals $\mathbf{r}_\lambda(\Omega, \Omega_0)$ in (11), which is the modeled value of HDRF from LUT. A_λ denotes the BHR, $[A_\lambda(\Omega_0)]$; $\Phi(\mathrm{LAI}, A_\lambda)$ is the solution distribution function mentioned in Section II-B, and N is the number of view directions used in the calculations. This function corresponds to a fixed sun angle, therefore, Ω_0 is omitted.

A_λ is given in the case of MISR. Equation (12) does not exceed retrieved uncertainties. For the POLDER data, we must solve (12) in order to evaluate $\Phi(\mathrm{LAI}, A_\lambda)$ and A_λ. The value of A_λ, which minimizes (12), can be expressed as (13), shown at the bottom of the next page.

Notations are similar to Section II-A. From (13), BHR's for each spectral band can be estimated from measured HDRF's. The resulting BHR values are a function of the solution distribution function, i.e., $\Phi(\mathrm{LAI}, A_\lambda) \equiv \mathrm{LAI}$. Then, we execute the first MISR comparison test in order to obtain the second iteration of $\Phi(\mathrm{LAI}, A_\lambda)$. One repeats this process until (12) does not exceed a threshold value.

B. Accuracy of BHR Evaluation

The accuracy of BHR evaluation described above was assessed as follows. For a given biome and a sun-view geometry, BHR's and HDRF's were calculated from LUT entries. For example, we choose grasses and cereal crops, a sun angle of 30°, and nine view directions distributed evenly over the hemisphere. For each combination of LAI and soil pattern, the corresponding BHR and HDRF values were regarded as true values. Then multi-view angle HDRF's with noise added to the test HDRF's were used as input to evaluate the BHR. Table V shows root mean square errors (RMSE) for two spectral bands at different noise levels. The RMSE is less than 7% for noise levels around 20%. Errors in the red band are larger than for the near-infrared band because the reflectance in red is less than in near-infrared. The BHR method was further validated as follows.

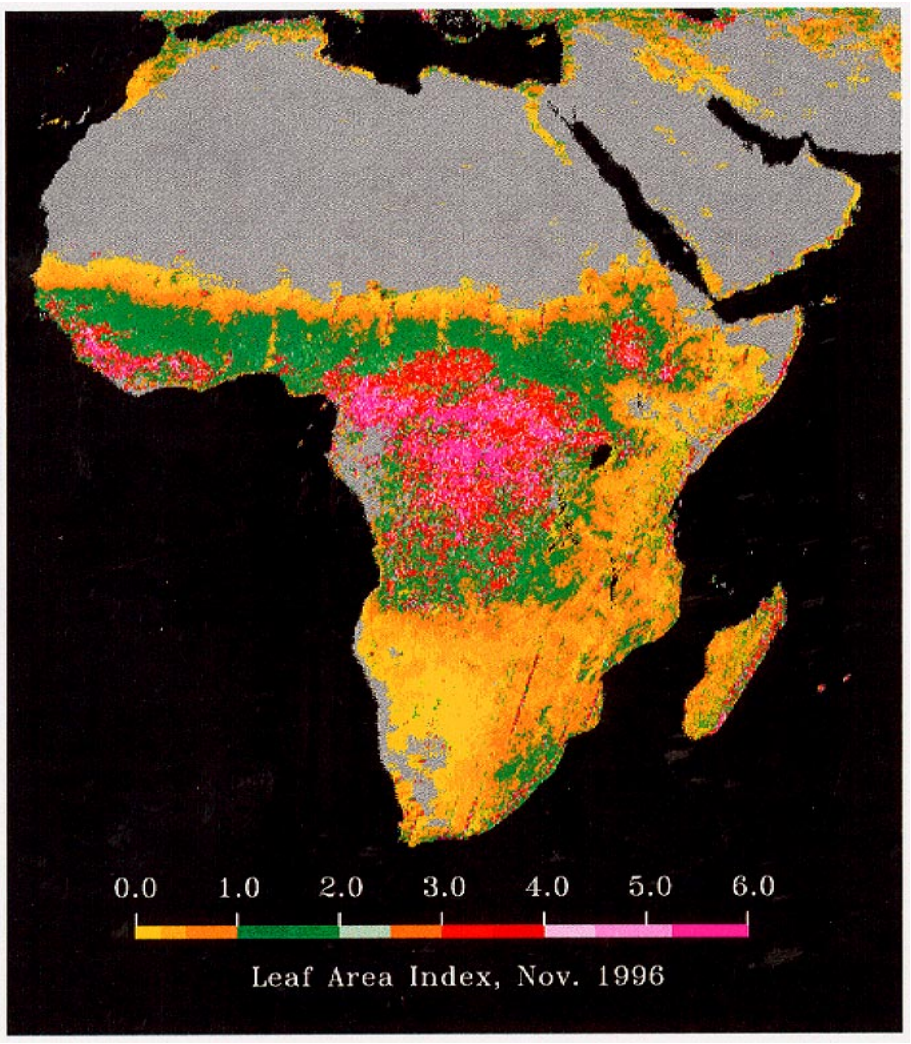

Fig. 11. LAI retrieved from POLDER data over Africa in November, 1996. The POLDER data is based on maximum NDVI selection, and the algorithm is executed in multi-angle case. For the unsuccessful pixels, the NDVI-LAI relationships shown in Fig. 7 were used to estimate LAI. Gray color in the image indicates either barren lands or that the data are not available.

A canopy radiation model based on the numerical solution (the discrete ordinates method) of the radiative transfer equation [20], applicable to the grasses and cereal crops, was used to simulate the HDRF's as well as BHR's in the red and near-infrared wave bands for different values of LAI and solar zenith angles (Table VI). The sensor zenith and relative azimuth angles were selected randomly within a range of 0 to 60° for the polar angle and 0 to 360° for the azimuth. Then, the entire hemisphere was sampled. The simulated HDRF's at 12 view directions were used to evaluate the BHR's exercising the method described earlier. A total of 210 test calculations were performed. The estimated and model simulated BHR's are compared and the RMSE of this test is shown in the last column of Table V. The error is equivalent to a 30% noise level from the first test. In general, errors are larger in the red band due to low canopy reflectance.

C. Histograms of LAI and NDVI

With the BHR method, the MISR LAI/FPAR algorithm can be run with the two-test process. Here, we took grasses and cereal crops as an example to investigate the algorithm behavior. The calculations were performed as follows: 1) one view angle only (near-nadir direction) with the HDRF test only (see Section IV); 2) 12 view angles with the HDRF test only; and 3) all available HDRF measurements to first estimate BHR and then with the BHR test only.

The distribution of retrieved LAI is shown in the upper left panel in Fig. 10. The single-angle HDRF test retrieval yeilds higher values of LAI than the other two tests. The BHR test results in the lowest LAI values. However, its distribution is similar to the ten-year average LAI distribution over Africa for the same time period reported by Myneni *et al.* [16].

$$A_\lambda = \frac{\sum_{k=1}^{N} \int d\Phi(\mathrm{LAI}, A_\lambda) w_{S,\lambda} [\mathbf{r}_\lambda(\Omega, \Omega_0) + (w_{S,\lambda} - w_{\mathrm{bs},\lambda}) \mathbf{r}_{\mathrm{bs},\lambda}(\Omega_0)]}{\sum_{k=1}^{N} \int d\Phi(\mathrm{LAI}, A_\lambda (w_{S,\lambda})^2} \tag{13}$$

The upper-right panel shows the distribution of NDVI from successful pixels. Clearly, the results for all cases are similar because the majority of data is successfully retrieved. For the case of HDRF single-angle test, the RI is 99.3%. In the case of HDRF multi-angle test, the RI is 83.6%, lower than the single-angle case because it is a more stringent test. For the case with the BHR test only, the RI is 96.8%. Presumably, the BHR's include information from multi-angle data and thus are more informative than the single-angle case.

The lower-left panel in Fig. 10 shows the NDVI distribution for unsuccessful pixels. Compared to the single-angle test resulting in algorithm failure at low NDVI values, the multi-angle test has more unsuccessful pixels at high NDVI values. In the case of the former, it is reasonable that low NDVI values correspond to bare ground, and high NDVI values correspond to reflectances which do not satisfy the uncertainty tolerance level. The unsuccessful pixels are distributed over the entire range, but cluster more around a NDVI of 0.4–0.6 for the multi-angle test. The NDVI of unsuccessful pixels is concentrated at a high NDVI value range (0.6–0.8) for the BHR test. This is similar to the single-angle case, as high NDVI's usually correspond to low red reflectances, which have high uncertainties.

VI. Conclusions

Results from prototyping of the MISR LAI/FPAR algorithm with POLDER data over Africa demonstrate the ability to produce global LAI and FPAR fields using multi-angle data. An image of LAI field over Africa in November, 1996 derived from POLDER data is shown in Fig. 11. Instead of using empirical relationships between vegetation indices and land surface parameters LAI/FPAR, the algorithm is a radiative transfer-based synergistic approach. The algorithm uses information about spectral and angular surface reflectances and the associated uncertainties provided by the instrument to estimate LAI and FPAR. However, the quality of retrievals is dependent upon the quality of the worst spectral reflectance if uncertainties in spectral canopy reflectances are not available. Band and view direction-dependent uncertainties in atmospherically corrected surface reflectances is critical to improve the quality of the LAI/FPAR product. The use of multi-angle data decreases the dispersion and saturation of LAI, and increases the localization and quality of the retrieved LAI and FPAR fields. Although minimum dispersion of the retrieved solution distribution cannot be used to identify biome types with high accuracy, especially with coarse resolution observations, LAI and FPAR are still estimated with high accuracy. The expected MISR data have many advantages over POLDER data because MISR data has better atmospheric correction and less uncertainties. It has higher spatial resolution, which reduces the effect of biome mixtures and has wider angular coverage, which offers potentially more information. Therefore, the result of LAI/FPAR retrievals is expected to improve with the improvement of data quality. Finally, the method of BHR evaluation proposed in this paper shows the close relationship between BHR and HDRF measurements, and the efficient use of both observations will lead to better retrievals of the surface parameters.

Acknowledgment

The authors would like to thank O. Hautecœur and Centre National d'Etudes Spatiales/Centre d'Etudes Spatiales de la Biosphère (CNES/CESBIO) for providing the POLDER data used in this study.

References

[1] J. V. Martonchik, D. J. Diner, B. Pinty, M. M. Verstraete, R. B. Myneni, Y. Knyazikhin, and H. R. Gordon, "Determination of land and ocean reflective, radiative, and biophysical properties using multiangle imaging," *IEEE Trans. Geosci. Remote Sensing*, vol. 36, pp. 1266–1281, July 1998.

[2] D. J. Diner, J. V. Martonchik, C. Borel, S. A. W. Gerstl, H. R. Gordon, Y. Knyazikhin, R. Myneni, B. Pinty, and M. M. Verstraete, "MISR: Level 2 Surface Retrieval Algorithm Theoretical Basis," Calif. Inst. Technol., Jet Propulsion Lab., Pasadena, CA, JPL Int. Doc. D-11401, Rev. C, 1998.

[3] Y. Knyazikhin, J. V. Martonchik, D. J. Diner, R. B. Myneni, M. M. Verstraete, B. Pinty, and N. Gobron, "Estimation of vegetation canopy leaf area index and fraction of absorbed photosynthetically active radiation from atmosphere-corrected MISR data," *J. Geophys. Res.*, vol. 103, no. D24, pp. 32 239–32 256, 1998.

[4] M. Choulli and P. Stefanov, "Reconstruction of the coefficient of the stationary transport equation from boundary measurements," *Inv. Probl.*, vol. 12, pp. L19–L23, 1996.

[5] J. Ross, *The Radiation Regime and Architecture of Plant Stands*, W. Junk, Ed. Norwell, MA, 1981, pp. 253–281.

[6] Y. Knyazikhin, J. V. Martonchik, R. B. Myneni, D. J. Diner, and S. Running, "Synergistic algorithm for estimating vegetation canopy leaf area index and fraction of absorbed photosynthetically active radiation from MODIS and MISR data," *J. Geophys. Res.*, vol. 103, no. D24, pp. 32 257–32 275, 1998.

[7] D. J. Diner, G. P. Asner, R. Davies, Y. Knyazikhin, J. P. Muller, A. W. Nolin, B. Pinty, C. B. Schaaf, and J. Stroeve, "New directions in earth observing: Scientific application of multi-angle remote sensing," *Bull. Amer. Meteorol. Soc.*, vol. 80, no. 11, pp. 2209–2228.

[8] K. Stamnes, "Reflection and transmission by a vertically inhomogeneous planetary atmosphere," *Planet. Space Sci.*, vol. 30, pp. 727–732, 1982.

[9] K. M. Case and P. F. Zweifel, *Linear Transport Theory*. Reading, MA: Addison-Wesley, 1967.

[10] Y. Tian, Y. Zhang, Y. Knyazikhin, R. B. Myneni, J. M. Glassy, G. Dedieu, and S. W. Running, "Prototyping of MODIS LAI/FPAR Algorithm with LASUR and Landsat Data," *IEEE Trans. Geosci. Remote Sensing*, vol. 38, pp. 2387–2401, Sept. 2000.

[11] J. V. Martonchik, D. J. Diner, R. A. Kahn, T. P. Ackerman, M. Verstraete, B. Pinty, and H. R. Gordon, "Techniques for retrieval of aerosol properties over land and ocean using multiangle imaging," *IEEE Trans. Geosci. Remote Sensing*, vol. 36, pp. 1212–1227, July 1998.

[12] P. Y. Deschamps, F. M. Brèon, M. Leroy, A. Podaire, A. Bricaud, J. C. Buriez, and G. Seze, "The POLDER mission: Instrument characteristics and scientific objectives," *IEEE Trans. Geosci. Remote Sensing*, vol. 32, pp. 598–615, May 1994.

[13] W. B. Rossow and L. Garder, "Selection of a map grid for data analysis and archival," *J. Clim. Appl. Meteorol.*, vol. 72, pp. 2–20, 1991.

[14] M. Leroy, J. L. Deuzè, F. M. Brèon, O. Hautecœur, M. Herman, J. C. Buriez, D. Tanrè, S. Bouffies, P. Chazette, and J. L. Roujean, "Retrieval of atmospheric properties and surface bidirectional reflectances over land from POLDER/ADEOS," *J. Geophys. Remote Sensing*, vol. 102, no. D14, pp. 17 023–17 037, 1997.

[15] O. Hautecœur and M. Leroy, "Surface bidirectional reflectance distribution function observed at global scale by POLDER/ADEOS," *Geophys. Res. Lett.*, vol. 25, no. 22, pp. 4197–4200, 1998.

[16] R. B. Myneni, R. R. Nemani, and S. W. Running, "Estimation of global leaf area index and absorbed PAR using radiative transfer models," *IEEE Trans. Geosci. Remote Sensing*, vol. 35, pp. 1380–1393, Nov. 1997.

[17] F. G. Hall, J. R. Townshend, and E. T. Engman, "Status of remote sensing algorithms for estimation of land surface state parameters," *Remote Sens. Environ.*, vol. 51, pp. 138–156, 1995.

[18] P. J. Curran, "Multispectral remote sensing for the estimation of green leaf area index," *Phil. Trans. R. Soc. Lond. A*, vol. 309, pp. 256–270, 1983.

[19] M. M. Verstraete and B. Pinty, "Designing optimal spectral indexes for remote sensing application," *IEEE Trans. Geosci. Remote Sensing*, vol. 34, pp. 1254–1265, Sept. 1996.

[20] R. B. Myneni and J. Ross, Eds., *Photon-Vegetation Interactions—Applications in Optical Remote Sensing and Plant Ecology*. New York: Springer-Verlag, 1991, ch. 5, pp. 139–158.
[21] F. M. Brèon, V. Vanderbilt, M. Leroy, P. Bicheron, C. L. Walthall, and J. E. Kalshoven, "Evidence of hot spot directional signature from airborne POLDER measurements," *IEEE Trans. Geosci. Remote Sensing*, vol. 35, pp. 479–484, Mar. 1997.
[22] W. Qin and X. Yueqin, "On the hot spot effect of leaf canopies: Modeling study and influence of leaf shape," *Remote Sens. Environ.*, vol. 50, pp. 95–106, 1994.
[23] D. L. Jupp and A. H. Strahler, "A hot spot model for leaf canopies," *Remote Sens. Environ.*, vol. 38, pp. 193–210, 1991.
[24] M. Leroy and F. M. Brèon, "Angular signatures of surface reflectances from airborne POLDER data," *Remote Sens. Environ.*, vol. 57, pp. 97–107, 1996.
[25] W. Lucht, "Expected retrieval accuracies of bidirectional reflectance and albedo from EOS-MODIS and MISR angular sampling," *J. Geophys. Res.*, vol. 103, no. D8, pp. 8763–8778, 1998.
[26] D. J. Diner, L. M. Barge, C. J. Bruegge, T. G. Chrien, J. E. Conel, M. L. Eastwood, J. D. Garcia, M. A. Hernandez, C. G. Kurzweil, W. C. Ledeboer, N. D. Pignatano, C. M. Sarture, and B. G. Smith, "The multi-angle imaging spectroradiometer (AirMISR): Instrument description and first results," *IEEE Trans. Geosci. Remote Sensing*, vol. 36, pp. 1339–1349, July 1998.
[27] M. E. James and S. N. V. Kalluri, "The pathfinder AVHRR land data set: An improved coarse resolution data set for terrestrial monitoring," *Int. J. Remote Sensing*, vol. 15, pp. 3347–3363, 1994.
[28] T. R. Loveland, J. W. Merchant, D. O. Ohlen, and J. F. Brown, "Development of a land cover characteristic data base for the conterminous U.S.," *Photogramm. Eng. Remote Sensing*, vol. 57, pp. 1453–1463, 1991.
[29] R. B. Myneni, F. G. Hall, P. J. Sellers, and A. L. Marshak, "The interpretation of spectral vegetation indices," *IEEE Trans. Geosci. Remote Sensing*, vol. 33, pp. 481–486, Mar. 1995.
[30] T. N. Carlson and D. A. Ripley, "On the relation between NDVI, fractional vegetation cover, and leaf area index," *Remote Sens. Environ.*, vol. 61, pp. 241–252, 1997.
[31] R. B. Myneni and D. L. Williams, "On the relationship between FAPAR and NDVI," *Remote Sens. Environ.*, vol. 49, pp. 200–211, 1994.
[32] J. G. P. W. Clevers, "The application of a weighted infrared-red vegetation index for estimating leaf area index by correcting for soil moisture," *Remote Sens. Environ.*, vol. 29, pp. 25–37, 1989.
[33] J. M. Chen, "Canopy architecture and remote sensing of the fraction of photosynthetically active radiation absorbed by boreal conifer forests," *IEEE Trans. Geosci. Remote Sensing*, vol. 34, pp. 1353–1368, July 1996.
[34] J. M. Chen and J. Cihlar, "Retrieving leaf area index of boreal conifer forests using landsat TM images," *Remote Sens. Environ.*, vol. 55, pp. 153–162, 1996.

Yu Zhang received the B.S. degree in physics from the Tsinghua University, Beijing, China, in 1994 and the M.S. degree in electronics from Peking University, Beijing, in 1997. He is currently pursuing the Ph.D. degree in the area of remote sensing and vegetation land surface study in the Department of Geography, Boston University, Boston, MA, working on developing, prototyping, and validating the synergistic algorithm of LAI and FPAR estimation for the MODIS and MISR projects.

His research interests are multi-angle remote sensing and radiative transfer models in vegetation canopies.

Yuhong Tian received the B.S. degree in meteorology from Nanjing Institute of Meteorology, Nanjing, China, in 1992 and the M.S. degree in meteorology from the Chinese Academy of Meteorological Sciences, Beijing, China, in 1995. She is currently pursuing the Ph.D in the Department of Geography, Boston University, Boston, MA, working on prototyping and validating the synergistic algorithm of LAI and FPAR estimation of the MODIS projects.

Her research interests include scale issues in remote sensing and modeling radiative transfer in vegetation canopies.

Yuri Knyazikhin received the M.S. degree in applied mathematics from Tartu University, Tartu, Estonia, in 1978, and the Ph.D. degree in numerical analysis from the N.I. Muskhelishvilli Institute of Computing Mathematics, Georgian Academy of Sciences, Tbilisi, Georgia, in 1985.

From 1978 to 1990, he was a Research Scientist with the Institute of Astrophysics and Atmospheric Physics and the Computer Center of the Siberian Branch of the Russian Academy of Sciences, Tartu University. He was with the University of Göttingen, Göttingen, Germany, from 1990 to 1996. He is currently a Research Associate Professor, Department of Geography, Boston University, Boston, MA. He has worked and published in areas of numerical integral and differential equations, theory of radiation transfer in atmospheres and plant canopies, remote sensing of the atmosphere and plant canopies, ground-based radiation measurements, forest ecosystem dynamics, and modeling sustainable multifunctional forest management.

Dr. Knyazikhin was an Alexander von Humboldt Fellow from 1992 to 1993.

John V. Martonchik received the B.S. degree in physics from Case Institute of Technology, Cleveland, OH, in 1964 and the Ph.D. degree in astronomy from the University of Texas, Austin, in 1974.

He joined the Jet Propulsion Laboratory (JPL), Pasadena, CA, in 1972 and currently is a Research Scientist. His experiences include telescopic and spacecraft observations of planetary atmospheres, laboratory and theoretical studies of the optical properties of gaseous, liquid, and solid materials, and the development and implementation of one- and three-dimensional radiative transfer and line-by-line spectroscopy algorithms for studies of planetary atmospheres and Earth tropospheric remote sensing. He has been a Co-Investigator on several NASA programs and is the Algorithm Scientist for aerosol and surface retrievals on the EOS Multi-angle Imaging Spectro Radiometer (MISR) experiment.

Dave J. Diner received the B.S. degree in physics (Hons.) from the State University of New York, Stony Brook, in 1973, and the M.S. and Ph.D. degrees in planetary science from the California Institute of Technology, Pasadena, in 1977 and 1978, respectively.

He has been with the Jet Propulsion Laboratory (JPL), Pasadena, since 1978, first as a National Research Council Resident Research Associate, then as a contractor with Ball Aerospace, and since 1981, as a JPL employee. He is currently Member of Technical Staff and Leader of the Multi-angle Imaging Science Element in Earth and Space Sciences Division. He has been involved in numerous NASA planetary and Earth remote sensing investigations, and is presently Principal Investigator of the EOS Multi-angle Imaging Spectro Radiometer (MISR) experiment and its airborne counterpart, AirMISR.

Marc Leroy received the Ph.D. degree in 1980 from the Paris VII University, Paris, France, in the field of radiatively driven stellar winds.

He was a Research Associate of the Observatoire de Paris, Paris, France, in 1981 and worked in the field of theoretical plasma physics of the Earth's bow shock, both at the Observatoire de Paris, the University of Maryland, College Park. He joined the French Space Agency, Centre National d'Etudes Spatiales (CNES), Toulouse, France, in 1985 to work on calibration activities associated with the SPOT program, and in 1989 became the Head of the Department of Image Quality in the Image Processing Division, CNES Technical Center, Toulouse. He joined LERTS, now the Centre d'Etudes Spatiales de la Biosphère (CESBIO), Toulouse, in 1993, with a specific interest in the physics of remote sensing measurements in the optical domain. He is Principal Investigator on several major satellite remote sensing scientific programs (POLDER, VEGETATION, METEOSAT 2nd Generation), and is in charge of the development of algorithmic chains of land surface products of the POLDER instrument. He has authored over 40 peer-reviewed papers in the scientific literature.

Ranga B. Myneni received the Ph.D. degree in biology from the University of Antwerp, Antwerp, Belgium, in 1985.

Since 1985, he has been with Kansas State University, Manhattan, the University of Göttingen, Göttingen, Germany, and NASA Goddard Space Flight Center, Greenbelt, MD. He is currently on the Faculty of the Department of Geography, Boston University, Boston, MA. His research interests are in radiative transfer, remote sensing of vegetation, and climate–vegetation dynamics. He is also a MODIS and MISR science team member.